ACSNANO

www.acsnano.org

ARTICLE

Lifetime and Stability of Silicon Nitride Nanopores and Nanopore Arrays for Ionic Measurements

Yung-Chien Chou,[‖] Paul Masih Das,[‖] Dimitri S. Monos, and Marija Drndić*

Cite This: https://dx.doi.org/10.1021/acsnano.9b09964

Read Online

ACCESS | Metrics & More | Article Recommendations | Supporting Information

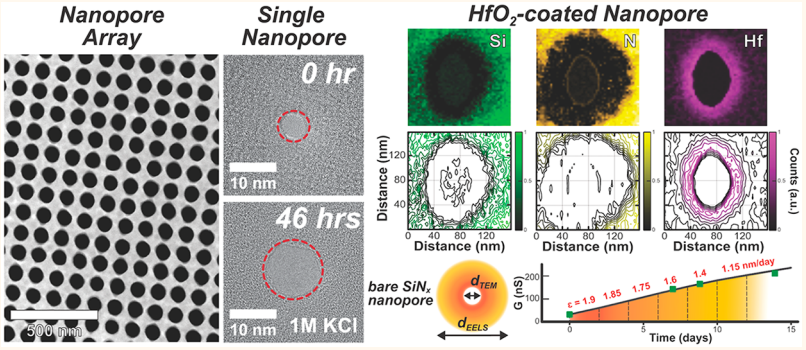

ABSTRACT: Nanopores are promising for many applications including DNA sequencing and molecular filtration. Solid-state nanopores are preferable over their biological counterparts for applications requiring durability and operation under a wider range of external parameters, yet few studies have focused on optimizing their robustness. We report the lifetime and durability of pores and porous arrays in 10 to 100 nm-thick, low-stress silicon nitride (SiN_x) membranes. Pores are fabricated using a transmission electron microscope (TEM) and/or electron beam lithography (EBL) and reactive ion etching (RIE), with diameters from 2 to 80 nm. We store them in various electrolyte solutions (KCl, LiCl, $MgCl_2$) and record open pore conductance over months to quantify pore stability. Pore diameters increase with time, and diameter etch rate increases with electrolyte concentration from $\Delta d/\Delta t \sim 0.2$ to ~ 3 nm/day for 0.01 to 3 M KCl, respectively. TEM confirms the range of diameter etch rates from ionic measurements. Using electron energy loss spectroscopy (EELS), we observe a N-deficient region around the edges of TEM-drilled pores. Pore expansion is caused by etching of the Si/SiO_2 pore walls, which resembles the dissolution of silicon found in minerals such as silica (SiO_2) in salty ocean water. The etching process occurs where the membrane was exposed to the electron beam and can result in pore formation. However, coating pores with a conformal 1 nm-thick hafnium oxide layer prevents expansion in 1 M KCl, in stark contrast to bare SiN_x pores (~ 1.7 nm/day). EELS data reveal the atomic composition of bare and HfO_2-coated pores.

KEYWORDS: *solid-state nanopore, silicon nitride, nanoporous membranes, nanopore array, electron beam lithography, electron energy loss spectroscopy*

Nanopore-based biomolecule, DNA, and nanoparticle analysis is a single-molecule and single-particle technique that potentially offers orders of magnitude faster and more economical detection, counting, and analysis than current methods.[1,2] This includes DNA length measurement, specific sequence detection, single-molecule dynamics, and *de novo* sequencing as well as counting and sizing of nanoscale particles.[3−7] The basic concept involves using an applied voltage to drive the particle through a nanopore, which separates chambers of electrolyte solution. This voltage also drives a flow of electrolyte ions through the pore, measured as an electric current. When molecules pass through the nanopore, they block the flow of ions, and thus their structure and length can be determined based on the degree and duration of the current reductions.[8]

Received: December 18, 2019
Accepted: April 10, 2020
Published: April 10, 2020

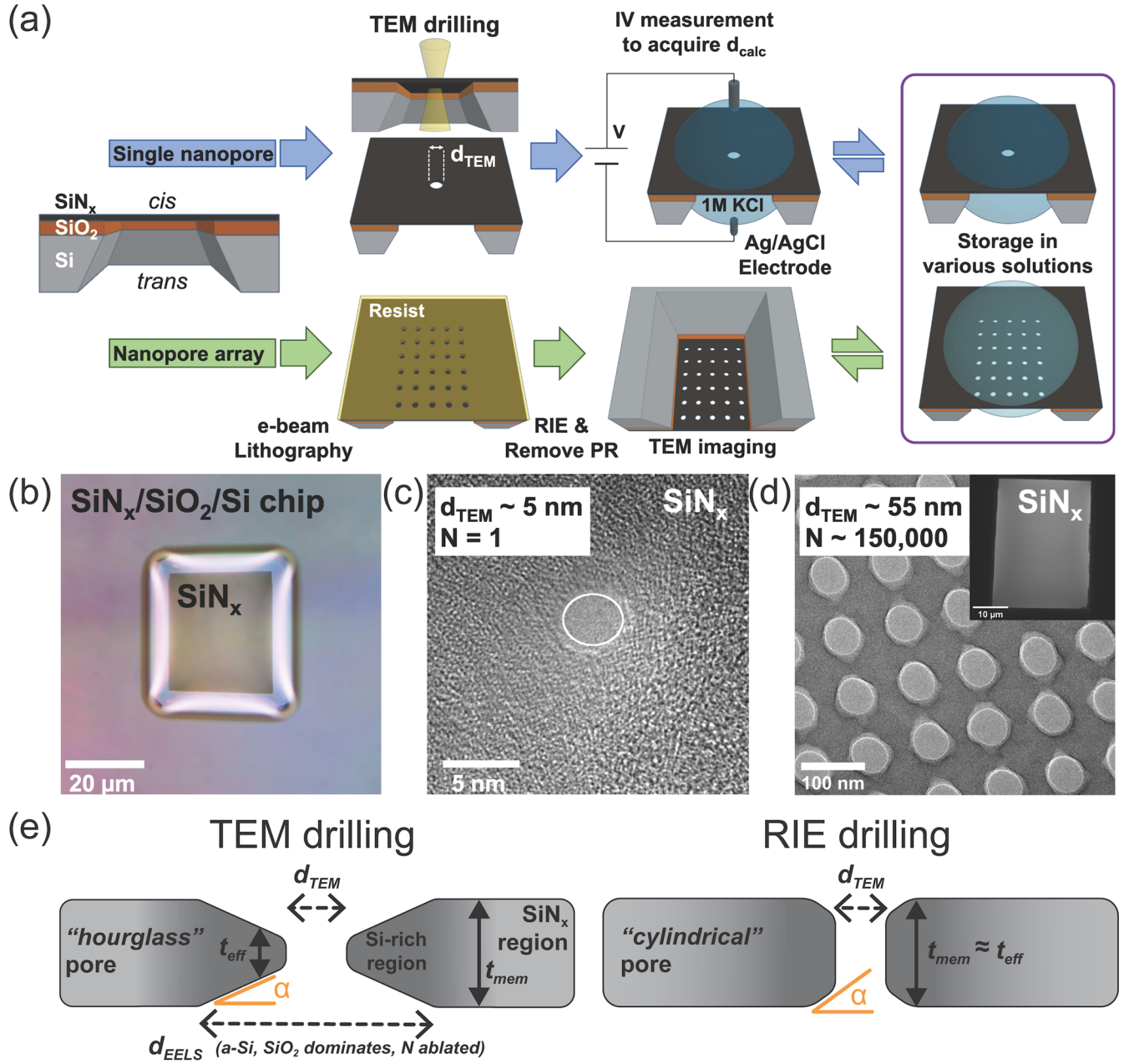

Figure 1. Schematic and images of two nanopore fabrication methods. (a) Schematic showing the fabrication process of (blue arrow) individual nanopores using TEM drilling and (green arrow) nanopore arrays using EBL and RIE. After fabrication, TEM-drilled nanopores are first measured to acquire initial conductance and stored in various salt solutions for a period of time, then ionic measurements are repeated to record the following conductance. Nanopore arrays as fabricated are inspected with TEM to acquire initial diameter, d_{TEM}. Repeated TEM inspections are conducted after storage in salt solutions to acquire corresponding d_{TEM}. (b) Optical image of $SiN_x/SiO_2/Si$ chip with a suspended SiN_x membrane. (c) TEM image of a single SiN_x nanopore with $d_{TEM} \sim 5$ nm. (d) TEM image of a nanopore array with $d_{TEM} \sim 55$ nm. (Inset) Low-magnification TEM image demonstrates the nanopore array covered the whole suspended SiN_x membrane with $N \sim 150{,}000$. (e) Schematic of final pore shape for the two processes described in (a). (Left) TEM drilling results in an hourglass-shaped pore due to the Gaussian-like nature of the electron beam (see Figure 3), while (right) RIE creates a more cylindrical pore (see Figure 4).

Silicon nitride (SiN_x) pores, first fabricated around 2003 using electron and ion beam drilling of thin SiN_x membranes,[3,9] have proven robust and useful in biomolecular detection measurements and are excellent candidate pores for future diagnostic and filtering devices.[10,11] Compared to biological protein-based pores, solid-state pores offer a wider range of tunable diameters, more scalable fabrication, and higher robustness for environmental applications. Similarly, compared to newer two-dimensional (2D) membranes such as graphene,[12] SiN_x has a superior thermal stability and is employed in a wide range of industrial applications. While focus has been on obtaining high signal-to-noise ratios[13] in ionic experiments by thinning pores and optimizing nanopore chips by adding insulating layers, quantifying the durability of these pores has received little attention, and at best, the insights on this topic are scattered within the literature[14−16] as secondary comments or even contradictory. Because of the particular promise of silicon nitride pores, we focus this study on them and report a quantification and improvements of their lifetime and durability.

https://dx.doi.org/10.1021/acsnano.9b09964
ACS Nano XXXX, XXX, XXX−XXX

In this report, we first demonstrate the fabrication of single nanopores by transmission electron microscope (TEM) drilling and nanopore arrays by electron beam lithography (EBL) and reactive ion etching (RIE), which contain up to hundreds of thousands of nanopores, with high fidelity, in thin SiN_x membranes. By measuring their diameters in two different ways, by calculating diameter, d_{calc}, from ionic measurements on single pores and by directly measuring the diameter from TEM images of single pores and nanopore arrays, d_{TEM}, we quantify the stability of pores placed under typical nanopore operating/storage conditions. We used several salt solutions such as KCl, LiCl, and $MgCl_2$ and characterize the pores over long periods of time (up to ~ 2 months) and subsequently characterize the effects of salt solutions on SiN_x pore geometry, pore diameter etch rates (up to ~ 3 nm/day), and ionic transport properties. We confirm quantitative findings from ionic measurements by direct high-resolution transmission electron microscope imaging of both TEM-drilled and EBL fabricated nanopores, confirming the range of pore expansion rates from ionic measurements.

In addition to pore expansion, this etching phenomenon can be exploited for pore formation with selective electron irradiation. As the irradiated section of the SiN_x membrane etches away in salt solution, we observe how a nanopore emerges in the thinnest spot of that region. Electron energy loss spectroscopy (EELS) in an aberration-corrected TEM provides 2D spatial composition maps that give insights into the chemical structure of these pores. TEM-drilled pores exhibit a thinned ring around the pore in which N is depleted, leaving a Si/SiO_2-rich region that dissolves in salt solutions at ambient conditions, resulting in slow, long-term pore expansion. For nanopore arrays, we detect SiO_2 at the pore walls, but a less extended Si-rich region, as this fabrication process involves top-down etching of the resist-patterned SiN_x membrane. From EELS, we infer that the etching process for both types of pores involves SiO_2 dissolution and resembles the slow dissolution process of silicon found in minerals such as silica (SiO_2) and silicates in seawater.

Finally, we tested several surface coatings and present a viable route for mitigating the chemical etching and expansion of nanopores through atomic layer deposition (ALD) of hafnium oxide. We find that a very thin (~ 1 nm-thick) coating of SiN_x pores with hafnium oxide completely prevents long-term pore expansion, offering a practical solution to fabricating stable and robust nanopores. EELS 2D spatial maps further reveal how ALD coating affects the previous TEM-drilled pore structure.

Practical aspects like fabrication standards, nanopore durability, and reproducibility of results are crucial questions yet to be directly addressed and quantified before solid-state nanopores can be properly evaluated and possibly improved, to become a viable technology. By quantifying the highly environment-dependent properties of SiN_x nanopores, the results presented here set some limits of SiN_x pores to be accounted for in practical applications and lead the way for future studies on maximizing the lifetimes and longer-term reusability of solid-state nanopores toward increasing robustness and lowering the cost of nanopore platforms.

RESULTS AND DISCUSSION

Nanopore Fabrication. Figure 1 demonstrates the fabrication of single nanopores and nanopore arrays in suspended SiN_x membranes. The 5 mm square silicon platforms (light gray) coated with 5 μm of SiO_2 (orange), unless noted otherwise (see Figure 3a), and a 10 and 20 nm-thick layer of low-stress SiN_x are first produced through conventional microfabrication techniques (Figure 1a).[11,17] As shown in the top row of Figure 1a (blue arrow), single nanopores are formed in TEM imaging mode by focusing the transmission electron beam onto the SiN_x membrane for 5−10 s (total dose ~ 8.0×10^{11} e^-/nm^2). Here, we utilize a high-resolution mode TEM operating at 200 kV with a beam current of 20 nA. By providing real-time feedback through TEM imaging, this technique allows the formation and observation of pores with precise diameters, d_{TEM}.[18]

The workflow for nanopore arrays fabricated by e-beam lithography is demonstrated schematically in the bottom row of Figure 1a (green arrow). A similar approach was reported in 2018 for fabricating nanopores in freestanding graphene and SiN_x membranes.[19] $Si/SiO_2/SiN_x$ chips are first coated with a ZEP520A polymer resist. With dots-on-the-fly electron beam lithography (EBL),[20] pore arrays are patterned onto a 50 μm square region. After resist development, RIE with trifluoromethane and oxygen (CHF_3/O_2) is utilized for SiN_x removal in the exposed circular regions to define the pores. By tuning the shot pitch to 100 nm, the highly perforated membrane still retains its structural integrity without collapsing.

Figure 1b shows the optical image of a suspended SiN_x window where pores are fabricated. Example TEM images are shown of a single pore (d_{TEM} ~ 5 nm) in a t_{mem} = 10 nm SiN_x membrane (Figure 1c), and a nanopore array (d_{TEM} ~ 55 nm) consisting of N ~ 150,000 pores in a t_{mem} = 100 nm SiN_x membrane (Figure 1d). The stoichiometry of these SiN_x membranes was determined using EELS[15] showing a ratio of Si:N ≈ 3:4 ($x \approx 1.3$). The as-fabricated pore diameters ranged from ~ 2 to 80 nm for single nanopores and ~ 50 to 60 nm for nanopore arrays. Two common models of pore structure are shown in Figure 1e. These variations are caused by the nature of fabrication process, which will be later discussed and confirmed by EELS.

While it has been observed among experimentalists that thin nanopores can expand over continuous usage and/or repeated operating conditions (*e.g.*, high-voltage and high-concentration salt solution for DNA translocations),[14] to the best of our knowledge, we are not aware of any systematic study to quantify these changes, yet, at this stage of the nanopore field, such studies are vital for future practical applications.

Definitions of Diameter and Thickness. We define the membrane thickness, t_{mem}, measured by ellipsometry after fabrication. We also define the nanopore thickness as "*effective thickness*", t_{eff}, in conjunction with the TEM-measured diameter, to match the measured conductance value from a simple conductance equation,[11,21] eq 1. For approximately cylindrical pores, $t_{eff} \approx t_{mem}$, as shown in Figure 1e. For hourglass-shaped pores, $t_{eff} = 1/3\ t_{mem} < t_{mem}$ fit well to the measured ionic conductance of TEM-drilled SiN_x pores.[11,22] The hourglass-shaped pore structure, in which $t_{eff} = 1/3\ t_{mem} < t_{mem}$, was confirmed by TEM tomography and is also consistent with measured conductance through TEM-drilled pores.[15,22−26]

We define two diameters, d_{TEM}, measured from TEM images, a top-down view onto the nanopore; d_{TEM} is the diameter corresponding to the smallest constriction within the pore. The error in d_{TEM} is ± 0.1 nm. The other, d_{calc}, is the pore diameter calculated from ionic conductance assuming an effective thickness, t_{eff}. We note that both approaches serve as good, but not ideal, estimates of the nanopore diameter, and both have corresponding sources of errors and limitations. The value of d_{TEM} corresponds to the pore size when it is in vacuum; the pore

https://dx.doi.org/10.1021/acsnano.9b09964
ACS Nano XXXX, XXX, XXX−XXX

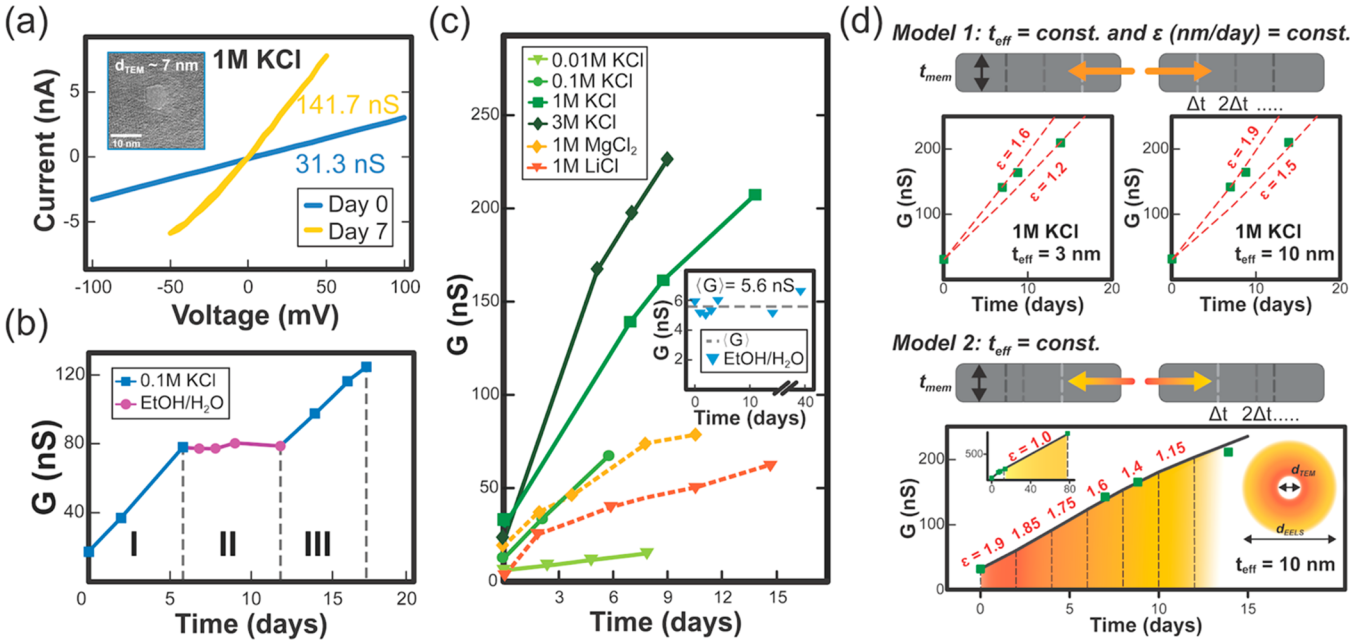

Figure 2. Ionic conductance measurement data from eight TEM-drilled pores (total of eight chips, each containing one pore). (a) Current–voltage curves for a single nanopore before and after storage in 1 M KCl over a course of 7 days, inset shows the nanopore TEM image, with d_{TEM} ~ 7 nm. Following measurement data are shown in (c). (b) G *vs* time for one single nanopore is shown in three regions. The pore was stored first in (I) 0.1 M KCl, then (II) ethanol/water (v/v = 1/1), then back to (III) 0.1 M KCl. This pore expanded from d_{calc} ~ 3–5 nm (beginning of I) to d_{calc} ~ 14–18 nm (end of region III). (c) G *vs* time for a total of seven single nanopores. Six different pores are stored in four different concentrations of KCl, 1 M $MgCl_2$, and 1 M LiCl. Conductance, *G*, is measured over a period of time. *I*–*V* measurement is performed in the control solution, 1 M KCl, pH 8.0, σ = 11.1 S/m. Inset shows a different pore, stored in ethanol/water, conductance remains stable over 40 days with $\langle G \rangle$ = 5.6 nS and d_{calc} = 2.6 ± 0.1 nm. (d) (Top) Proposed geometric model assuming constant pore thickness, t_{eff}, and diameter etch rate, ε. Given a fixed t_{eff}, a range of diameter etch rates (red dashed lines) are calculated to include the measured *G* (green squares) when the pore was stored in 1 M KCl. (Bottom) To further accommodate our observation of decreasing increment of conductance over time, we propose another geometric model assuming constant pore thickness, t_{eff}, with varying diameter etch rate over time, when the diameter of pore is smaller than d_{EELS}. The fitting line was the result of calculated conductance with diameter etch rates varying every 2 days, starting with ε = 1.9 nm/day, and later decreased to ε = 1.15 nm/day after 10 days. Assuming the diameter of pore exceeds d_{EELS} after 12 days, ε is then set to be constant, 1 nm/day. Inset shows our acquired *G* value up to 78 days of storage in 1 M KCl (see Table S1), overlaid with the fitting line from Model 2.

can change in size or close[27] over time after exposure to air and ionic solutions. The calculated diameter, on the other hand, represents a more relevant estimation at the time of the ionic measurements, but its value (from eq 2) depends on the assumed value of the pore thickness.

Ionic Measurements on Single-Pore Chips with TEM pores. To prepare nanopores for ionic measurements, both single nanopores and nanopore arrays are cleaned with boiling piranha solution, which removes organic contaminants from the SiN_x surface and aids in pore wetting (Figure 1a).[28] Etch rates of piranha for silicon and silicon nitride for micromachining processing are typically listed as 0 nm/min or "etch rate known to be slow or zero, but etch rate not measured", but further studies are needed to quantify its effect on SiN_x nanopore size.[29,30] No additional piranha cleanings were performed throughout the measurements.

Long-term pore durability over days and weeks is characterized by their stable ionic conductance *via* two-terminal current–voltage measurements on single pores and by subsequent TEM imaging of single pores and nanopore arrays. The conductance *G* for a nanopore with diameter *d* and effective thickness, t_{eff}, can be estimated from

$$G = \frac{I}{V} = \sigma\left[\frac{4t_{eff}}{\pi d^2} + \frac{1}{d}\right]^{-1} = \frac{\sigma\pi d^2}{4t_{eff} + \pi d} \quad (1)$$

where *I* is the measured ionic current, *V* is the applied voltage, and σ is the ionic solution conductivity.[31] Current–voltage (*I*–*V*) curves were measured in the control 1 M KCl (pH 8.0, with measured σ = 11.1 S/m). Every few (2–5) days, the pores were rinsed in DI water to remove residue from the storage solution and then dried with nitrogen gas before measuring their conductance in the control 1 M KCl solution. The conductance measurements lasted < 30 min over which time the pore conductance was constant, and from which the updated nanopore diameter values were calculated from

$$d_{calc} = \frac{G}{2\sigma}\left(1 + \sqrt{1 + \frac{16\sigma t_{eff}}{G\pi}}\right) \quad (2)$$

It has been shown that high-voltage pulses (up to ± 20 V) can form and expand nanopores in pristine SiN_x membranes.[32] We therefore limit the applied voltage to 0.1 V to minimize pore expansion due to voltage application[32] and to isolate the effects of electrolyte solution on pore size and performance. By calculating diameters at later times, we obtain diameter etch rates, $\Delta d_{calc}/\Delta t$, from conductance.

An ionic measurement of a single nanopore is shown in Figure 2a. As shown in the inset TEM image, the initial pore diameter after drilling was d_{TEM} ~ 7 nm. After storing in 1 M KCl solution for 7 days, the measured conductance increased from 31.3 nS to 141.7 nS. Assuming $t_{eff} = t_{mem}$ = 10 nm, corresponding d_{calc}

https://dx.doi.org/10.1021/acsnano.9b09964
ACS Nano XXXX, XXX, XXX–XXX

increased from 7.6 nm to d_{calc} = 20.6 nm. If we replace the effective thickness to t_{eff} = 1/3 t_{mem},[17] we obtain a slightly different calculated diameter increment, from d_{calc} = 5.2 to 16.1 nm. Taking both t_{eff} into account, we then acquire a range of rate, $\Delta d_{calc}/\Delta t$ = 1.6 to 1.9 nm/day. Following measurement data are shown in Figure 2c.

Figure 2b shows ionic conductance measured in control 1 M KCl solution as a function of storage time (alternatingly stored in 0.1 M KCl and ethanol/water) for another pore with an initial diameter $d_{TEM} \sim$ 3 nm and corresponding d_{calc} = 3.5 nm (assuming t_{eff} = 3 nm) and d_{calc} = 5.3 nm (assuming t_{eff} = 10 nm). The d_{calc} increased approximately linearly when the pore was stored for a week in 0.1 M KCl at an average rate, $\langle\varepsilon\rangle_{T=7\text{days}}^{t_{eff}=3\text{nm}}$ = 0.9 ± 0.1 nm/day and $\langle\varepsilon\rangle_{T=7\text{days}}^{t_{eff}=10\text{nm}}$ = 1.2 ± 0.1 nm/day, respectively (regions I and III), while the conductance, and therefore pore diameter, remained constant when the pore was stored in ethanol/water for a week (region II).

We define $\langle\varepsilon\rangle_T^{t_{eff}} = \langle\Delta d_{calc}/\Delta t\rangle_T^{t_{eff}}$ as the time-averaged diameter change per unit time, that is, the "average diameter etch rate" over time period T (in days); it was estimated as the average value of calculated diameter etch rates measured from consecutive ionic measurements on single pores. Consecutive ionic measurements were performed on single TEM-drilled pores at day 0 (t = 0) and then up to about day 78 (*e.g.*, days 1, 7, 9, 14). Individual diameter etch rates (*e.g.*, ε_1 to ε_3) are estimated from repeated conductance measurements on the same pore over time, relative to the initial I–V measurement on day 0, as

$$\langle\varepsilon\rangle_T^{t_{eff}} = \left(\sum_{n=1}^{N-1}\varepsilon_n\right)/(N-1) = \frac{\sum_{n=1}^{N-1}\left(\frac{d_{calc,n}-d_{calc,0}}{t_n-t_0}\right)}{N-1} \quad (3)$$

where $d_{calc,n} - d_{calc,0}$ is the calculated diameter change during the time period $t_n - t_0$, t_{eff} is the assumed effective pore thickness, and N is the total number of ionic I–V measurements (N = 5), yielding $N - 1$ rates, ε_1 to ε_{N-1}. Here, $d_{calc,0}$ is the diameter calculated from the initial conductance value at t = 0. I–V measurements were performed for up to T = 15 days for most pores (Figure 2c) and up to T = 40 days (inset of Figure 2c). Errors for diameter etch rates are quoted as the deviations from mean values. We quote average diameter etch rates, but note that the slope of G *vs* time decreases in time. We later discuss and model this slowdown of etching at long times.

Figure 2c shows the same measurements of conductance *vs* storage time for six additional different single-pore chips with initial diameters, d_{calc}, in the range of ~ 2–8 nm (assuming t_{eff} = 10 nm). Data are shown for four different concentrations of KCl solution (0.01, 0.1, 1, and 3 M), 1 M solutions of LiCl and $MgCl_2$, and (inset) ethanol/water. From measurements on single pores, we observe five main characteristics of this etching process:

(i) *Conductance increased over time in salt solutions.* The pore expands due to interactions between the salt solution and pore wall.

(ii) *Conductance increased more rapidly for higher concentrations of KCl.* This phenomenon can be explained by a gradual pore wall etching by the salt solution which proceeds faster in more concentrated solutions. It is important to observe that this happens even without external stimulation, for example, voltage or laser light. From data in Figure 2c, we extract average diameter etch rates, of $\langle\varepsilon\rangle_T^{t_{eff}=10\text{nm}}$ = 0.21 ± 0.01, 1.2 ± 0.1, 1.7 ± 0.2, and 2.9 ± 0.3 nm/day for 0.01, 0.1, 1, and 3 M KCl solution, respectively. These average rates correspond to the expansions of four different individual pores, soaked in solutions with four different KCl concentrations, and the errors quoted above are the deviation from the mean of diameter etch rates from three to five consecutive measurements on a single pore over time (up to 15 days).

(iii) *Conductance increased slower in LiCl and $MgCl_2$ than in KCl.* For example, from the data for two pores plotted in Figure 2c, we see that pore diameter also increased in 1 M LiCl and 1 M $MgCl_2$, at rates of $\langle\varepsilon\rangle_T^{t_{eff}=10\text{nm}}$ = 1.3 ± 0.6 and 0.8 ± 0.2 nm/day, respectively, about two times slower than in 1 M KCl. The varying diameter etch rates between 1 M salt solutions of KCl, LiCl, and $MgCl_2$ could result from the differences in the activity of the electrolyte ions in aqueous solutions, indicated by the value of the activity coefficient, γ.[33] The activity coefficient for a specific ion is known to depend on and differ from its counterion in a single electrolyte solution. Anionic activity coefficients, γ_{Cl^-}, for 1 M KCl, LiCl, and $MgCl_2$ at 298 K have been reported to be 0.664, 0.517, and 0.453, respectively.[34−36] We empirically observe that the diameter etch rate is proportional to the square of the anionic activity coefficient, $\varepsilon \propto \gamma_{Cl^-}^2$: the ratio of diameter etch rates $\varepsilon_{KCl}:\varepsilon_{LiCl}:\varepsilon_{MgCl_2}$ = 1:0.59:0.47, and is in excellent agreement with the corresponding ratios for $\gamma_{Cl^-}^2$, 1:0.61:0.47. For 1 and 3 M KCl, the anionic activity coefficients, γ_{Cl^-}, are reported[34] to be similar. However, our calculated diameter etch rates are about 1.7 and 2.9 nm/day and indicate that for higher concentrations the diameter etch rate is higher. A similar trend was reported by Yamazaki *et al.*,[16] where a higher concentration KCl solution shortens the time needed to thin the membrane and form a pore. With that being said, we cannot conclude here a simple correlation between anionic activity coefficient and concentration. However, our reported work provides crucial guidance toward future studies on detailing the correlations between higher concentration and diameter etch rates.

(iv) *Conductance did not change in ethanol/water solution.* For the two pores stored in ethanol/water solution, conductance remained stable. The inset of Figure 2c illustrates this on one pore with $\langle G\rangle$ = 5.6 nS and d_{calc} = 2.6 ± 0.1 nm, which was characterized for 40 days. Another example is in Figure 2b (Region II).

(v) *We observe a decreasing rate of conductance increment in time, that is, a decreasing first derivative, $\Delta G/\Delta t$.* The slope of G *vs* t decreases in time for all the curves measured. This is most likely due to the change in structure (Figure 2d) and chemistry (Figure 3d) around the edge of the pore.

Practical Geometric Models for Conductance, $G(t)$, *vs* Time. We present two useful geometrical models, illustrated in Figure 2d, to view this process and to fit to the conductance data, $G(t)$, in Figure 2c.

Model 1: Constant Pore Thickness (t_{eff} = const.) and Constant Diameter Etch Rate (ε = const.). Without precise thickness monitoring for the pore throughout measurement, a good first assumption is that the effective nanopore thickness, t_{eff}, falls between t_{eff} = 1/3 $t_{mem} \approx$ 3 nm, and the full membrane thickness, t_{eff} = $t_{mem} \approx$ 10 nm, due to the hourglass shape of

https://dx.doi.org/10.1021/acsnano.9b09964
ACS Nano XXXX, XXX, XXX−XXX

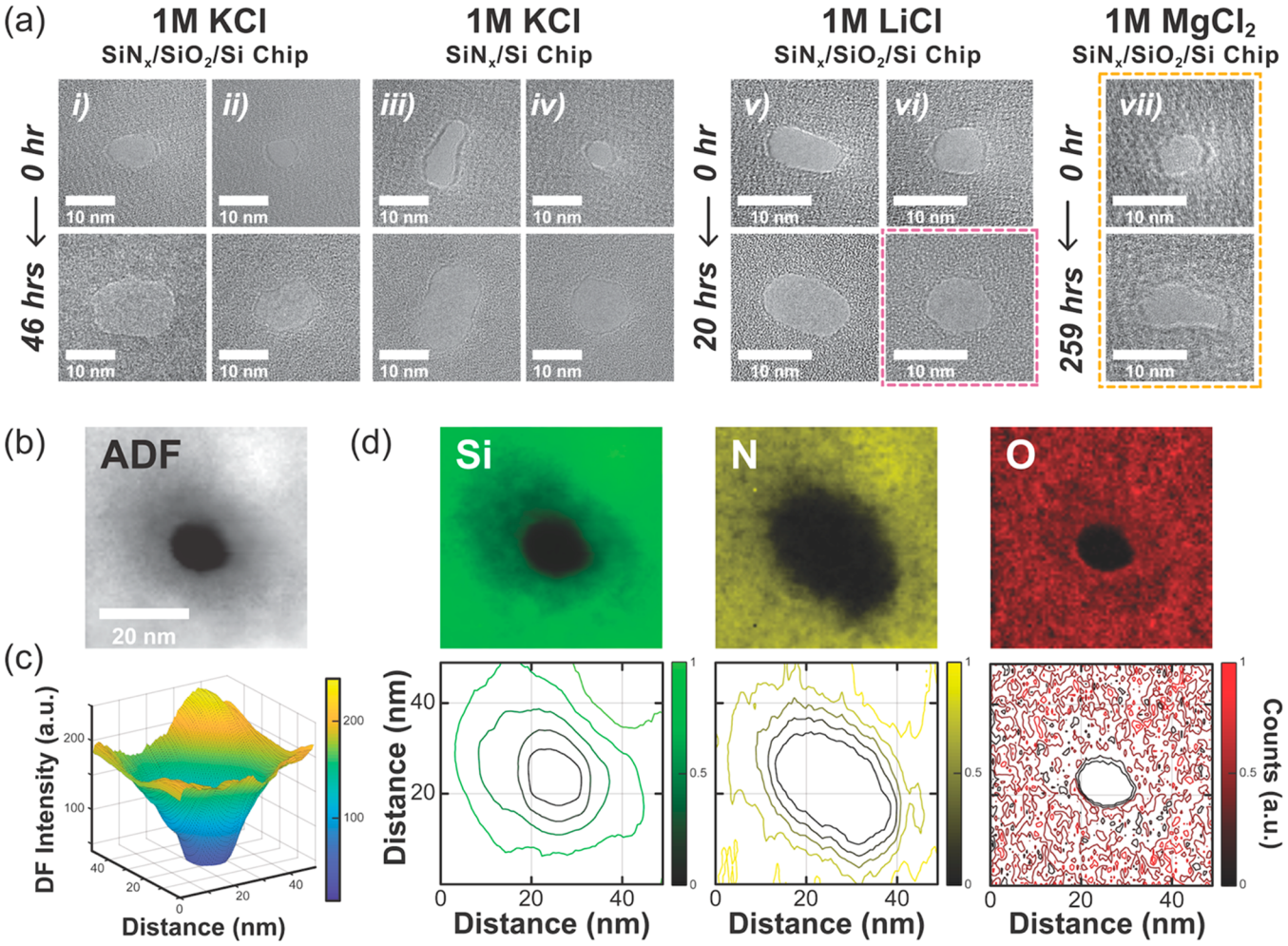

Figure 3. TEM imaging of pores before and after storage in various salt solutions with structural (ADF) and chemical (EELS) characterization. (a) Images of (top row) various TEM-drilled pores in a 10 (pore vii) and 20 (pores i–vi) nm-thick SiN_x membrane. The bottom row are images of the same pores with the same orientation after storage in (i, ii) 1 M KCl, (iii, iv) 1 M KCl (membrane containing no SiO_2) for 46 h, (v, vi) 1 M LiCl for 20 h, and (vii) 1 M $MgCl_2$ (as in Figure 2c) for 259 h. While pores etch, they maintain their original shape (*i.e.*, circular or elliptical) and expand isotropically. (b) ADF image of a single TEM-drilled pore and a (c) 3D map of ADF intensity (pore vi in (a), outlined by purple dashed square). (d) 2D EELS spatial intensity maps of the (green) Si $L_{2,3}$, (yellow) N K, and (red) O K edges at ~ 100, 400, and 530 eV, respectively. The bottom row shows contour maps as a function of normalized EELS signal intensity. Due to electron beam exposure, TEM-drilled pores display a Si-rich, N-deficient region around the pore edge with a diameter of 20–30 nm.

TEM-drilled pores.[17] We therefore calculated the predicted conductance *vs* time lines with the same starting G = 31.3 nS as the pore stored in 1 M KCl (Figure 2a), but with different constant diameter etch rates $\langle\varepsilon\rangle$ ranging from 1.2 to 1.9 nm/day for t_{eff} = 3 and 10 nm in Figure 2d. G as a function of time is given by

$$G(t) = \frac{\sigma\pi d^2}{4t_{eff} + \pi d} = \frac{\sigma\pi(d_o + \langle\varepsilon\rangle t)^2}{4t_{eff} + \pi(d_o + \langle\varepsilon\rangle t)} = \frac{\sigma}{\pi}\frac{f^2(t)}{B + f(t)} \quad (4)$$

where $f(t) = \pi(d_o + \langle\varepsilon\rangle t)$, and $B = 4\,t_{eff}$. The measured conductance values corresponding to 1 M KCl fall in between lines for t_{eff} = 3 and 10 nm with $\langle\varepsilon\rangle_{T=15\text{days}} \approx 1.6$ nm/day, which is similar to the previous calculation for the other pore in Figure 2c.

Under these conditions and from a satisfactory match with the measured conductance over time, it seems reasonable to assume, as the simplest model, that the pore is expanding in diameter, while its thickness remains roughly constant. To further directly study the changes in the thickness of suspended membranes, two 20 nm-thick SiN_x pristine chips without nanopores were immersed in 1 M KCl for more than 7 and 25 days separately. We find that changes in thickness of these two pristine SiN_x membranes are mostly negligible over time and < 0.5 nm. The thickness was measured with a Filmetrics F40 interference system, and both measurements show a goodness of fit of > 94%, by comparing the recorded refractive index as a function of wavelength to the known database for $Si_3N_4/SiO_2/Si$ thin-film profile measurements. This result directly supports our estimations of diameter etch rate using a fixed initial thickness (t_{eff} = const.) and further indicates that the exposed SiN_x around the pore edges plays a key role for the etching process.

Model 2: Constant Pore Thickness (t_{eff} = const.) and Time-Dependent Diameter Etch Rate, $\varepsilon(t)$. The model of increasing pore diameter and constant pore thickness explains the overall magnitude of conductance increase but fails to explain the slowing down of the conductance increase in time, seen by the downward curving of G *vs* time (in days) in Figure 2c. Our observations can be explained by assuming a diameter etch rate, $\varepsilon(t)$, that decreases in time, and we obtain a better match with our data, compared to the constant ε model (Model

https://dx.doi.org/10.1021/acsnano.9b09964
ACS Nano XXXX, XXX, XXX–XXX

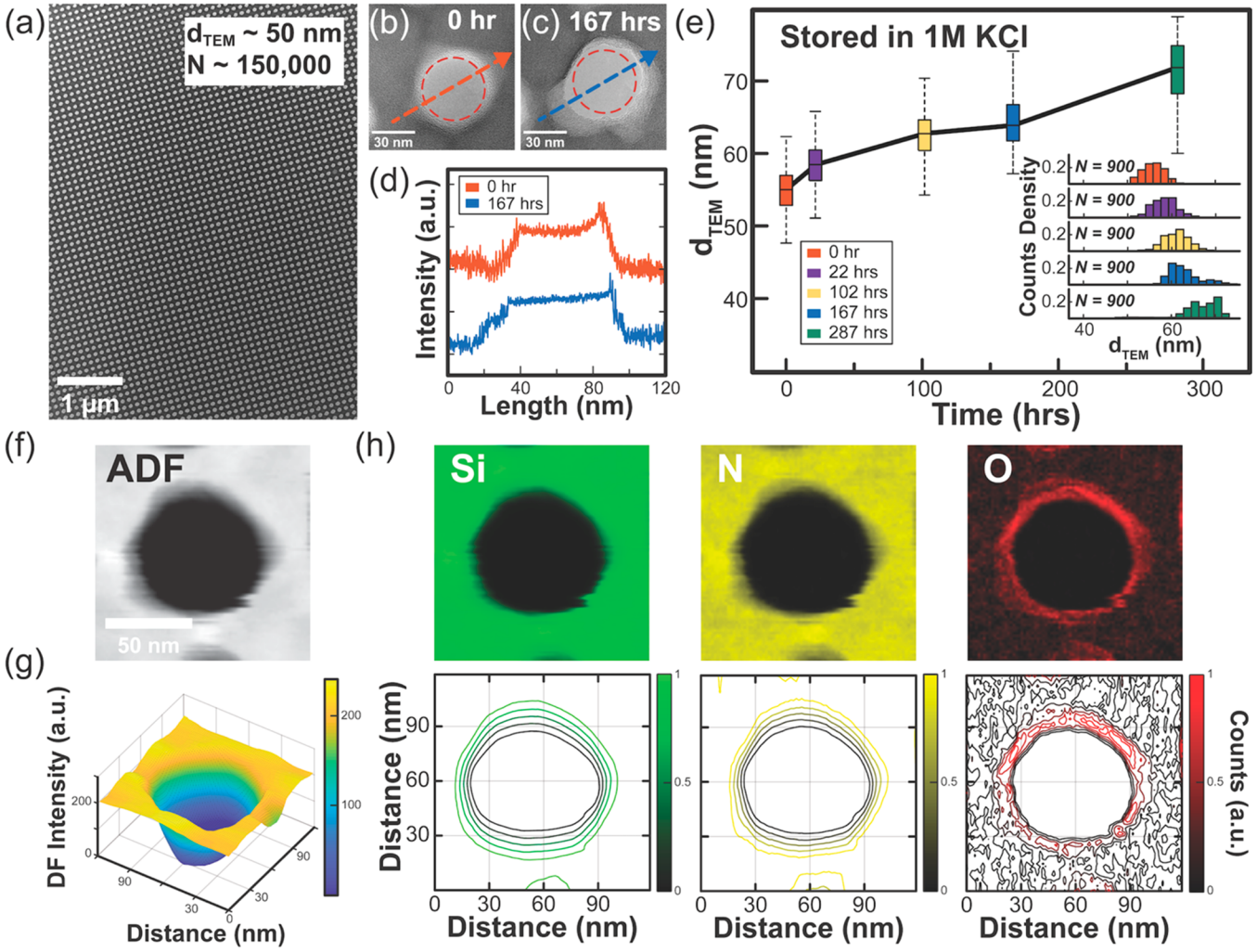

Figure 4. TEM imaging, time-dependent etching in 1 M KCl, and EELS data from a nanopore array chip made by EBL and RIE. (a) TEM image of the as-fabricated SiN_x nanopore array, fabricated *via* EBL and RIE. (b) Two TEM images of two different nanopores within this array with diameters close to the mean diameter of the distribution, chosen from the array right after fabrication, and (c) after the array was stored in 1 M KCl for 167 h. A red dashed circle in (b) outlines the pore region, and the same circle is plotted in (c) to visually illustrate how the typical pores grew after etching, together with (d) TEM intensity line scan profiles of these two different pores shown along the orange (0 h) and blue (167 h) arrows in (b) and (c), respectively. We note that tracing the same pore over time was difficult, and we show two representative pores with diameters close to the mean of the distributions, to visually illustrate the average pore expansion in the array. (e) Normalized boxplot of d_{TEM} distributions from a series of nanopore array images over time for 900 randomly chosen nanopores. For each histogram/time, the 900 pores were chosen randomly from the center (> 5 μm away from the edge) of the membrane (see Figure S5 for more details). Inset shows five histograms of the measured d_{TEM} distributions over time after 0, 1, 4, 7, and 12 days. (f) ADF image of a single RIE pore and a (g) 3D map of ADF intensity. (h) 2D EELS spatial intensity maps of the (green) Si $L_{2,3}$, (yellow) N K, and (red) O K edges at ~ 100, 400, and 530 eV, respectively. The bottom row shows contour maps as a function of normalized EELS signal intensity. Pores formed through EBL and RIE exhibit a more confined Si-rich region and SiO_2-rich pore edge.

1). Figure 2d shows such a fit to $G(t)$ by allowing the diameter etch rate to gradually decrease from 1.9 nm/day to 1.15 nm/day over the first 12 days after immersion in 1 M KCl. Over longer periods of time (up to 2.5 months in 1 M KCl), we obtain a decreased diameter etch rate of ~ 1 nm/day, as shown in the inset of Figure 2d.

Finally, in addition to the changing diameter, we also note that the effective nanopore thickness could also be changing in the range ~ 3−10 nm. We tried several additional models and fits but obtain diameter etch rate values bound by Model 1 which already assumes two scenarios for pore thicknesses, 3 and 10 nm. More importantly, time-dependent pore thickness fits alone fail to explain the slowing down of the diameter etch rate in time and the shape of G *vs* t, and one needs to invoke a time-dependent $\varepsilon(t)$ (Model 2).

Diameter (d_{TEM}) Estimation from TEM Imaging and EELS Analysis of TEM Pores. In addition to conductance measurements, we used TEM imaging to characterize single pores before and after storage in ionic solutions (without conductance measurements). TEM images provide direct measurements of d_{TEM} as a function of storage time and allow for calculations of diameter etch rate, $\Delta d_{TEM}/\Delta t$. Figure 3a shows TEM images of seven individual pores before and after storage in various 1 M salt solutions. The images taken after salt solution exposure have been aligned to the same orientation before exposure to demonstrate any nonuniformities in the etching process. Pores drilled in TEM are typically round due to

https://dx.doi.org/10.1021/acsnano.9b09964
ACS Nano XXXX, XXX, XXX−XXX

the circular nature of the electron probe. The presence of occasional astigmatism in the electron beam causes elliptical pores to form (*e.g.*, pores iii and v in Figure 3a). In both cases, storage in salt solution leads to isotropic etching of the pore, allowing it to expand while approximately maintaining its original shape. This isotropic etching is consistent across different ionic solutions, such as KCl (pores i–iv), LiCl (pores v and vi), and $MgCl_2$ (pore vii). We note that the shape and composition of the thinned region at the pore edge strongly influence isotropic or anisotropic expansion of the pore (discussed later in Figure 3d).

TEM images from pores i and ii (higher strain) and pores iii and iv (lower strain) in Figure 3a also demonstrate that etching in salt solution occurs regardless of strain in the SiN_x membrane. This is achieved by using two kinds of wafers, SiN_x/Si and SiN_x/SiO_2/Si, where the middle, 5 μm-thick SiO_2 layer makes the membrane more curved and introduces more strain.[37] Furthermore, we also tested a commercial 20 nm-thick SiN_x membrane (without the middle SiO_2 layer in the chip), manufactured by SPI Supplies (see Supplementary Figure S3), to examine the etching effect from the salt solution and potentially from a heated environment. We indeed observed similar isotropic pore expansions in 1 M KCl salt solution, demonstrating that etching effects are not unique to our membranes.

Pore vii in Figure 3a is an instance in which we performed both ionic measurements (shown in Figure 2c) and TEM imaging. From an initial diameter d_{TEM} = 5.8 nm, the pore later expanded into an elliptical shape (13 × 9.4 nm), with an effective diameter d_{TEM}^{eff} = 11.1 nm, after being immersed for 11 days in 1 M $MgCl_2$. We note that the identification and imaging of one small pore in the membrane without prefabricated markers on the surface present many challenges. However, in this particular case, we had an inherent structural feature on the membrane surface that we could use as a guide. From the corresponding *I*–*V* measurements, we obtain a similar change of the diameter from d_{calc} = 5.4 to 11.8 nm (see Supplementary Figure S2). Future studies could design membranes with suitable markers to perform many correlated TEM and ionic measurements on single pores.

To determine the chemical composition of TEM pores and these adjacent thinned regions, we perform atomic resolution analytical and structural characterization using aberration-corrected TEM. With EELS 2D mapping of core-loss excitations, we are able to probe the underlying chemistry of SiN_x pores. Figure 3b is an annular dark-field (ADF) image of pore vi from Figure 3a after 20 h of storage in 1 M LiCl solution. Since ADF STEM images contain mass-contrast information from scattered electrons, the dark ring around the edge of the pore in Figure 3b is indicative of a localized region that has been thinned. The appearance of this thinned area is most likely due to the Gaussian-like nature of the TEM beam, which causes the SiN_x region around the pore to be exposed to electrons during TEM drilling and is apparent in a three-dimensional (3D) map of ADF image intensity (Figure 3c). We note that the 3D maps in this work (Figures 3c, 4g, and 6b) are not directly indicative of pore shape, but rather their relative thickness as a function of spatial position. The first column in Figure 3d shows an EELS map of the Si $L_{2,3}$ edge (green) for the pore in Figure 3b, and the corresponding 2D contour profiles as a function of electron counts. The Si signature is strong on the bulk SiN_x membrane (*i.e.*, far away from the pore) and gradually decreases in the irradiated thinned region up to the edge of the pore. Conversely, an EELS map of the N K edge (yellow) indicates that the thinned region is largely N-deficient compared to the SiN_x membrane. This demonstrates that TEM beam exposure results in selective removal of N from the SiN_x membrane and is consistent with previous reports.[15] Puster *et al.*[38] estimated a damage radius of ∼ 75 nm in the TEM mode, which can be reduced in STEM mode.[38,39] In our case, we observe an approximately 20 nm (see Supplementary Figure S1) to 30 nm diameter N-deficient region. Crucially, it also suggests that the etching process in TEM-drilled SiN_x nanopores could be primarily driven by interactions between ionic solutions and the amorphous Si pore edge. A uniform signal of the O K edge (red) is seen across both the membrane and thinned region, which we attribute to the formation of a native oxide layer.[40]

While there may be several chemical reactions responsible for pore expansion and etching, the effect of salt solution on silicon and silicon oxide has been studied in great detail previously, especially in the environmental context of various ocean minerals.[41] For example, silicon oxide is relatively water insoluble compared to other minerals, and its concentration and slow release from silica minerals in seawater has been studied over a few decades.[41] Upon dissolution of SiO_2 the following equilibrium is established: $SiO_2 + 2H_2O \leftrightarrow H_4SiO_4$. Additionally, other intermediate etching reactions with Cl^- can take place such as in plasma etching of SiO_2.[30] Yamazaki *et al.* tried to explain their recent etching of SiN_x membranes to form pores in salt solutions upon laser illumination.[16] They hypothesized the transient Si–Cl bond in water, that is unstable and could be replaced by water molecules to form SiO_2, which is then dissolved at an increasing rate with increasing temperature. In another recent experiment similar to Yamazaki *et al.*,[16] Gilboa *et al.*[42] argued that etching of SiN_x is accelerated for Si-rich membranes and this favors the interpretation involving dissolution of SiO_2 that is sped up in higher pH and at elevated temperature resulting from laser illumination.[43−45] While these explanations are plausible, targeted experiments toward articulating specific chemical reactions and rates could be carried out in this specific context of nanopores. These previous works together with our study point to dissolution of SiO_2 and the role of Si-rich regions in SiN_x for pore etching, formation, and structure instability.

Diameter (d_{TEM}) Distribution from TEM Imaging and EELS Analysis of RIE Pores. In contrast to single nanopores, nanopore arrays over micron length scales are easily identified in phase contrast TEM images. We therefore implemented TEM imaging as a direct and primary means to precisely quantify the time-dependent diameters of nanoporous SiN_x arrays after storage in various solutions. Pore etching over time was also directly observed for large-scale nanopore arrays.

Figure 4a is a TEM image of the as-fabricated array on a 100 nm-thick SiN_x membrane, and Figure 4b,c shows high-magnification TEM images of one pore within this array, which were acquired before and after storage for 1 week in 1 M KCl solution. The red dashed circle outlines the edges of the initial pore after fabrication. Figure 4d further shows the line scans of pores in these two images. These are two different, randomly chosen pores with diameters close to the mean diameter of the distribution. They are representative of the respective distributions and used to visually illustrate the mean pore expansion in the array over time. In these experiments, we were not able to track individual nanopores, but rather quantify the overall distribution.

https://dx.doi.org/10.1021/acsnano.9b09964
ACS Nano XXXX, XXX, XXX–XXX

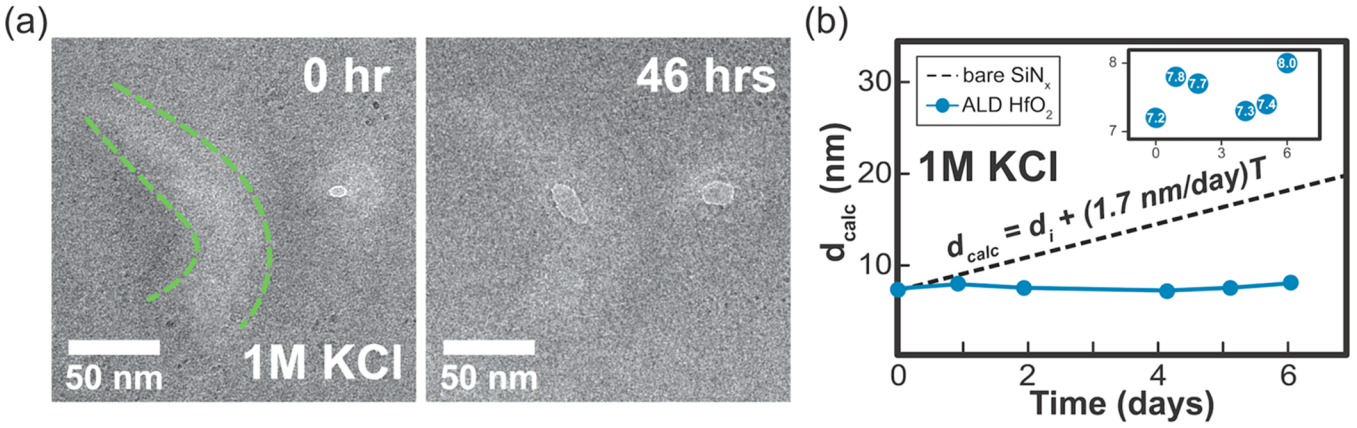

Figure 5. Fabrication of pores with electron beam thinning and resistance of HfO_2 coating to KCl etching. (a) TEM images of a 20 nm-thick SiN_x membrane (left) before and (right) after 46 h of storage in 1 M KCl solution. The dashed green lines indicate a thinned SiN_x region (containing no visible pores) formed with electron beam exposure. After KCl storage, a pore forms inside the thinned region, while the existing pore expanded as expected. (b) Time-dependent plot of d_{calc} for a (black line) bare TEM-drilled SiN_x pore and (blue line) HfO_2-coated SiN_x pore. Unlike the bare pore, the coated pore does not exhibit the same degree of expansion/etching over a period of 6 days.

These visual observations from TEM imaging are statistically supported. TEM images were processed using ImageJ software from which distributions of pore diameters, d_{TEM}, were characterized (see Methods section). In Figure 4e, we display the boxplot and histogram of all the TEM-measured nanopore diameters within one array and obtain the diameter etch rates from a randomly chosen subset of 900 pores on the chip. For each measurement, this subset of 900 pores was different but chosen within the same central area of the array. There is an inherent diameter spread across the SiN_x window due to fabrication limits, caused by the dome-shaped membrane structure. We therefore confined our imaging to a 20 μm × 40 μm area of the membrane from the center (see Supplementary Figure S5), where the standard deviation of the diameter distribution is less than 1.7 nm. We verified that the increase of average pore diameters observed over time is due to the etching, rather than intrinsic diameter variations from fabrication and how we sampled nanopores over the membrane. The diameter distributions in the inset of Figure 4e correspond to TEM images after the nanopore array was stored in 1 M KCl during ~ 1, 4, 7, and 12 days. Each distribution was normalized to 1 by summing the total of 900 randomly chosen pores. From the initial (d_{TEM} ~ 56 nm) and final average diameters (d_{TEM} ~ 69.3 nm) after 287 h, we estimate a diameter etch rate $\Delta d_{TEM}/\Delta t$ = 1.7 ± 0.9 nm/day, which agrees well with the value, $\langle \varepsilon \rangle_{T=15\text{days}}^{t_{eff}=10\text{nm}}$ = 1.7 ± 0.2 nm/day, obtained from TEM-drilled nanopores *via* ionic measurements in Figure 2c.

Figure 4f is an ADF image of one randomly chosen nanopore from the array in Figure 4a after 167 h of storage in 1 M KCl solution. In contrast to TEM pores, Figure 4g,h indicates that nanopores fabricated *via* EBL and RIE have a more confined N-deficient region, since the photoresist provides a robust protection from unwanted electron beam exposure and RIE results in highly anisotropic etching nature. Similar to results in Figure 3d, a uniform native oxide layer was observed across the membrane. This oxide also extends to the surface of the cylindrical pore wall (Figure 4g), leading to a strong O K edge signature in the EELS map (Figure 4h, red).

Observation of Pore Formation in Electron-Irradiated Membrane Areas in Salt Solution. When an intact (nonporous) SiN_x membrane region is exposed to electron irradiation, this region becomes Si/SiO_2 rich. This was proven by Puster *et al.*,[15] who continuously exposed small, 50 × 50 nm^2, regions of the SiN_x membrane to the electron beam in STEM mode and recorded EELS signals over time as the membrane became gradually thinner.[15] They monitored the Si and N signals and were able to deplete N completely, leaving a thin amorphous Si (a-Si) membrane behind.[15] Corresponding molecular dynamics simulations showed that such membranes can be thermodynamically stable down to ~ 0.7 nm-thick, and a-Si membranes as thin as 1−2 nm were made in this way.[15]

In our work, we further observe that an electron irradiated SiN_x membrane region, which is Si-rich and N-deficient,[15] slowly etches in salt solution over periods of hours and days, and the membrane thickness locally decreases. Figure 5a shows a single nanopore forming in an electron irradiated SiN_x region after about 2 days in 1 M KCl. The initial membrane here was t_{mem} = 20 nm. The region outlined by green dashed lines shows where the beam irradiated a small area of this membrane. Next to the irradiated region, we also drilled an ~ 10 nm-diameter pore. After 46 h in 1 M KCl, we imaged this region again and observed that a new pore emerged (d_{TEM} = 11.8 × 23.0 nm), while the initial pore expanded as expected (d_{TEM} increased from 10.4 to 13.8 nm).

With further studies and fine-tuning of this process, it may be possible that such simple wet etching of selectively irradiated membranes could be a useful way to make pores, especially if it is not critical to have precise sizes and pore shapes like TEM fabrication allows. This empirical tweaking of experimental parameters resembles the "*electroporation*" or "*membrane breaking*" approach to make pores, where a relatively high voltage (~ 10 V)[32] is used to break the membrane in salt solution in a few seconds or minutes, and where the salt type, concentration, pH, voltage magnitude, and time are empirically tweaked for a desired effect. Other recent reports of pore formation are variations on this theme, whereby additional optical and thermal excitation of the membrane was used to effectively thin it in a salt solution. For example, laser illumination of 2D membranes in salt solution was found to create pores and expand them at a rate on the order of ~ 0.1 nm/second due to photo-oxidation of the material.[39,46] One can think of this as "electroporation" aided by external parameters (such as presence of salt solution, temperature, illumination *etc.*), but at zero[46] or small applied voltages.[16,42,43,47] Yamazaki *et*

https://dx.doi.org/10.1021/acsnano.9b09964
ACS Nano XXXX, XXX, XXX−XXX

Table 1. Summary of Average Diameter Etch Rates Measured for Various Salt Solutions and Devices Discussed in the Text, Single Nanopores, and Nanopore Arrays Included[a]

storage solution[b]	measurement methods	t_{mem} (nm)	N (number of measurements)	storage duration, T (day)	$\langle\varepsilon\rangle_T^{t_{eff}=t_{mem}/3}$ (eq 3) (nm/day)	$\langle\varepsilon\rangle_T^{t_{eff}=t_{mem}}$ (eq 3) (nm/day)	$\Delta d_{TEM}/\Delta t$ (nm/day)
3 M KCl	$I-V$	10	4	9	2.6 ± 0.3	2.9 ± 0.3	N/A
1 M KCl	$I-V$	10	5	78	1.4 ± 0.2	1.7 ± 0.2	N/A
	TEM	20	6	1.9	N/A	N/A	1.9 ± 0.8
	TEM[c]	20	10	1.9	N/A	N/A	1.9 ± 0.3
	TEM[d]	100	5	12	N/A	N/A	1.7 ± 0.9
	TEM[e]	20	6	2	N/A	N/A	2.1 ± 0.1
0.1 M KCl	$I-V$	10	3	5	0.9 ± 0.1	1.2 ± 0.1	N/A
1 M LiCl	$I-V$	10	7	15	0.9 ± 0.4	1.3 ± 0.6	N/A
	TEM	20	18	0.8	N/A	N/A	1.4 ± 0.3
1 M $MgCl_2$	$I-V$/TEM	10	5/2	11	0.6 ± 0.2	0.8 ± 0.2	0.5 ± 0.2
0.01 M KCl	$I-V$	10	4	8	0.14 ± 0.01	0.21 ± 0.01	N/A
1 M KCl(with HfO_2)	$I-V$	10 + 2	6	6	0.3 ± 0.2	0.4 ± 0.3	N/A
	TEM	20 + 5	4	6	N/A	N/A	≈const.
$EtOH/H_2O$	$I-V$	10	7	40	0.0 ± 0.1	0.0 ± 0.1	N/A

[a]For single-nanopore data acquired from ionic measurements, errors are estimated using the average deviations from the mean values of $\langle\varepsilon\rangle_T^{t_{eff}}$, after measured conductance was fitted to eq 3. TEM imaging methods are employed for both some single nanopores and nanopore arrays. For nanopore arrays, errors are quoted as the standard deviations in the histograms of d_{TEM} distributions over time (Figure 4e). Number of measurements (N) indicates the number of times when an inspection was performed *via* $I-V$ and/or TEM. For HfO_2-coated pores, t_{mem} was estimated as a sum of the SiN_x membrane thickness and the deposition thickness. [b]Note: All samples are stored and measured under room temperature and ambient light (pH 8.0) unless further noted. [c]SiN_x/Si chip. [d]Nanopores are fabricated with RIE. Each measurement contains a randomly chosen subset of 900 pores on the chip. [e]Commercial SiN_x/Si chip from SPI supplies. Sample was stored for 2 days under room temperature and ambient light and for 1 h under heated 1 M KCl solution at 60 °C.

al.[16] reported pore formation due to localized SiN_x heating while shining a 532 nm laser light on a membrane in 4 M KCl along with a probing voltage of 0.01 V. Authors hypothesized that a photothermally assisted etching process in solution results in pores equally thin (∼ 1−3 nm) as electron beam and RIE-thinned membranes.[11,15,17] Similarly, Gilboa *et al.*[42] found that etching rates under laser illumination of amorphous SiN_x membranes in salt solution can be attributed to photochemical reactions that are highly sensitive to the initial Si:N ratio in the membrane. This body of recent work, taken in totality with our EELS data and observations of slow etching at ambient conditions without any applied voltage, strongly indicates that etching occurs because of Si-rich regions and helps establish a better mechanistic picture of SiN_x pores and their behavior. In our case, membrane exposure to TEM and RIE increases the relative ratio of Si:N at nanopore edges and makes that region susceptible to faster etching by salt solution then the rest of it. Future work can systematically vary SiN_x stoichiometry and address pore formation and properties. Such studies will be of increasing relevance as SiN_x pores enter commercial applications.

Surface Treatment and EELS Analysis of Hafnium-Oxide Coated Silicon Nitride Pores. While there may exist other more stable solid-state pore materials that could replace SiN_x, one distinct advantage of SiN_x pores for practical applications is that they show the highest signal-to-noise ratio for DNA measurements.[13,14] Furthermore, silicon nitride membranes are easily manufacturable, well-studied, improved, and established in industry. It is therefore beneficial to seek alternatives to prevent the SiN_x pore etching process and produce stable pores.

To this end, we have tested several surface modifications on the SiN_x pores by coating them from both sides (*cis* and *trans*), including Al_2O_3[48] and poly(ethylene glycol) (PEG).[28] In brief, these coated pores still etched at similar or higher rates than the bare SiN_x pores. However, we have discovered that when we coated the pores with a conformal 1 nm-thick layer of HfO_2 *via* ALD, the coated pores remained stable in size in 1 M KCl solution over days. This is consistent with recent observations reported by Yamazaki *et al.*,[16] where a coating of HfO_2 inhibited pore expansion under laser illumination for 10 min at 60 °C. In our measurements, a single nanopore was first drilled with d_{TEM} = 3.6 nm, cleaned with a 10 min piranha treatment, and then coated with 1 nm thick HfO_2, resulting in a total thickness of t_{eff} = 12 nm. During the five acquired data points over the course of 6 days, the measured conductance fluctuated slightly in between 31.5 ± 2.7 nS, corresponding to d_{calc} = 7.6 ± 0.4 nm, which remained virtually unchanged. In Figure 5b, a flat d_{calc} *vs* time trend is shown, from which we extract a diameter etch rate of essentially zero, $\langle\varepsilon\rangle_{T=6days}$ = 0.4 ± 0.3 nm/day, calculated from eq 1, for t_{eff} = 12 nm. Note that this rate is calculated relative to the initial diameter, d_{calc} (t = 0) = 7.2 nm and fails to reflect diameter increase and decrease between consecutive measurements (inset of Figure 5b). If we averaged over consecutive positive and negative diameter etch rates between successive measurements, the calculated rate would be 0.1 ± 0.3 nm/day.

These results demonstrate a stark difference compared to the much faster etching ($\langle\varepsilon\rangle_{T=15days}^{t_{eff}=10nm}$ = 1.7 ± 0.2 nm/day from Figure 2c) for bare SiN_x pores under identical conditions. The dashed line in Figure 5b indicates predicted d_{calc} for 1 M KCl. Thin HfO_2 coating therefore offers a practical and promising solution toward prolonged nanopore lifetime and robust nanopore fabrication for biosensing operating purposes.

Assuming etching Model 1 (see Figure 2d), we concluded from our experiments that an approximate, yet practical empirical equation can be used to predict the effective SiN_x pore diameter, d_{calc}, after storage for time T (in days) in ionic solution:

$$d_{calc,final} = d_{calc,initial}(t = 0) + \langle\varepsilon\rangle_T T \quad (5)$$

https://dx.doi.org/10.1021/acsnano.9b09964
ACS Nano XXXX, XXX, XXX−XXX

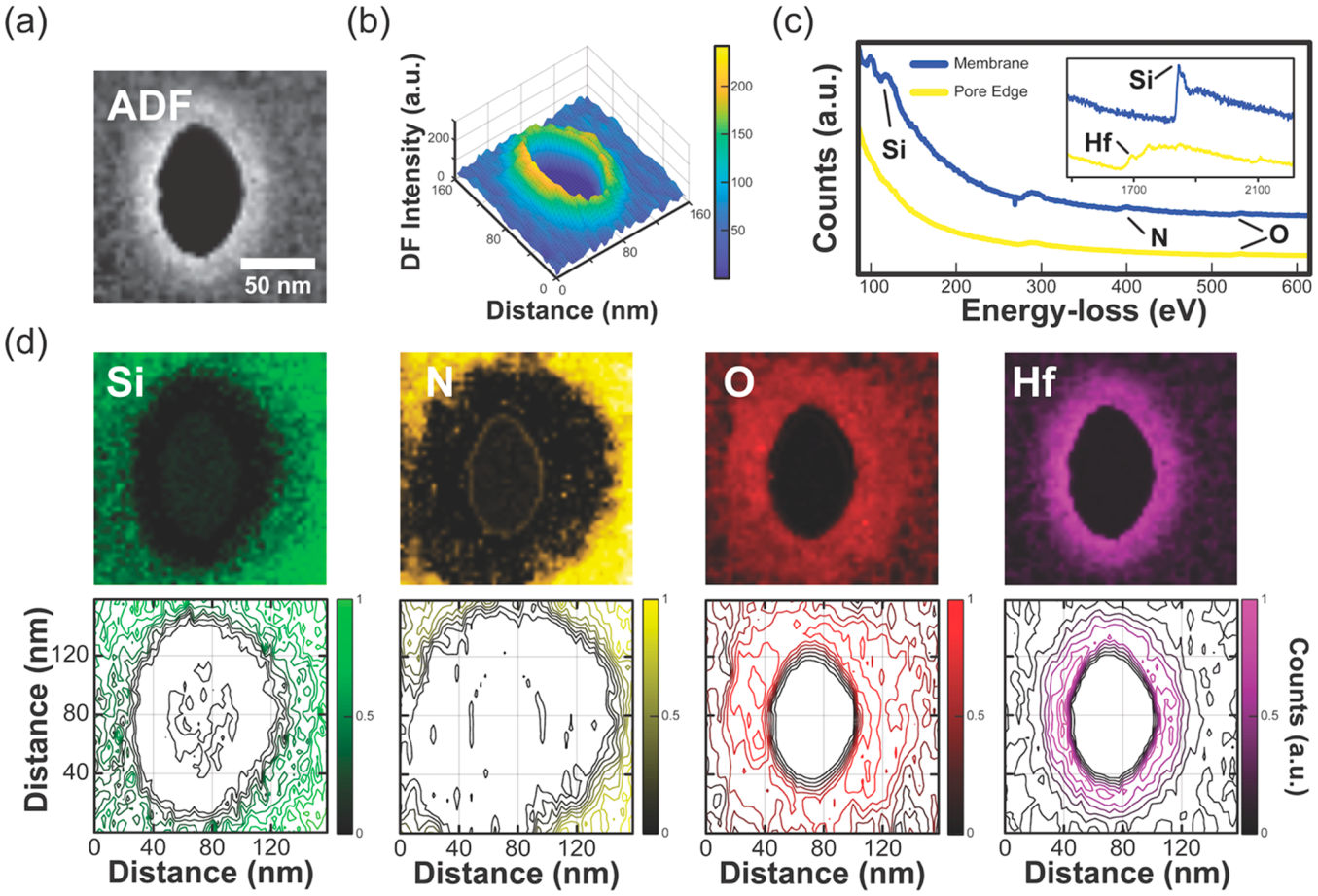

Figure 6. Chemical and structural characteristics of HfO_2-coated pores. (a) ADF image of a TEM-drilled SiN_x pore coated with 2.5 nm of HfO_2 *via* ALD. (b) 3D pore map based on ADF *Z*-contrast showing an increase in intensity/thickness at the pore edge. (c) EELS spot spectra taken on the (blue) bulk SiN_x membrane and (yellow) pore edge with prominent Si, N, O, and Hf edges labeled. (d) 2D EELS spatial intensity maps of the (green) Si K, (yellow) N K, (red) O K, and (purple) Hf M_4 edges at ~ 1850, 400, 530, and 1700 eV, respectively. The bottom row shows contour maps as a function of normalized EELS signal intensity. The ALD coating results in shrinkage of the TEM-drilled pore and a HfO_2-rich pore edge.

where $\langle\varepsilon\rangle_T$ is the time-averaged diameter etch rate in nm/day measured relative to the diameter at t = 0 when the pore is immersed in salt solution, and $d_{calc,initial}$ and $d_{calc,final}$ are the initial (t = 0) and final (t = T) diameters in nm. Table 1 summarizes all the time-averaged diameter etch rates over the indicated time periods, T, measured for different solutions and the numbers of measurements (I–V and/or TEM) per sample. All results are for ambient conditions and pH 8.0. From the recent studies using laser illumination to form pores,[16,42,46] we infer that these rates are likely to change for other parameters (pH, temperature, Si:N ratio in the membrane) which could be addressed by future studies. Importantly, the calculated diameter etch rates are similar from both the ionic measurements and direct TEM imaging, providing an overall picture of etching and the range of the etching rates. The diameter etch rates for small (d_{TEM} < 10 nm) and big (d_{TEM} > 50 nm) pores are similar (*e.g.*, Figures 3a and 4a), indicating that $\Delta d_{TEM}/\Delta t$ can be considered as approximately independent of the initial pore size.

Figure 6 demonstrates the nanoscale effects of ALD on the structure and chemical composition of TEM-drilled pores. The ADF image in Figure 6a is a pore that was initially drilled in a 20 nm-thick SiN_x membrane using TEM and then coated with 2.5 nm of HfO_2 *via* ALD. The 3D map of ADF intensity shown in Figure 6b indicates that the ALD coating results in a localized increase in thickness around the pore edge. This is in stark contrast to the thinned regions surrounding non-ALD-coated pores (see Figure 3b,c). Core-loss EELS analysis reveals the differences in composition between the pore edge and bulk SiN_x membrane. The blue EELS spectrum in Figure 6c was acquired on the bulk SiN_x membrane far (> 100 nm) away from the pore. It exhibits the Si $L_{2,3}$, N K, and Si K edges at ~ 100, 400, and 1850 eV, respectively, expected for SiN_x. Also present are C K and O K edges at ~ 280 and 530 eV due to hydrocarbon contamination and native oxide formation, respectively. The Si and N edges are noticeably absent in EELS spectra acquired at the pore edge (yellow spectrum in Figure 6c). The appearance of the O K edge at ~ 530 eV and Hf M_4 edge at ~ 1700 eV suggests that the ALD process causes HfO_2 deposition around the TEM-drilled pore, causing a reduction in diameter.

The four elemental EELS maps shown in Figure 6d demonstrate the extent to which the TEM-drilled SiN_x pore has been shrunk by the HfO_2 ALD coating. Maps of the Si K (green) and N K (yellow) signals in the first and second columns, respectively, of Figure 6d reflect the original diameter of the TEM-drilled pore (*i.e.*, before ALD) and indicate that the area surrounding the pore edge (see Figure 6a) is largely free of SiN_x. As described previously in Figure 3 for bare TEM-drilled pores, these maps also show the presence of a Si-rich, N-deficient

https://dx.doi.org/10.1021/acsnano.9b09964
ACS Nano XXXX, XXX, XXX–XXX

region around the original TEM-drilled pore edge. Essentially, the O K (red) and Hf M_4 (purple) maps reveal a pore edge region after ALD that is entirely HfO_2 with a strongly localized Hf signal between the original edge of the TEM-drilled pore. This circular area has a diameter of ~ 20 nm and corresponds directly to the circular region of increased thickness around the pore shown in Figure 6b. This indicates that ALD can be used to shrink the diameter of SiN_x pores by introducing an HfO_2 passivation layer that is highly resilient to etching in salt solutions.

CONCLUSIONS

In conclusion, by performing consecutive ionic conductance measurements at low voltages (up to 0.1 V) to probe the pore size and/or by repeated TEM imaging over time, we characterized the changes in the SiN_x nanopore size due to the effects of salt solutions at room temperature and ambient light. We found that the pores expand in typical electrolyte solutions and concentrations with rates varying from ~ 0.2 to 3 nm/day. Pore walls contain silicon oxide/silicon that can dissolve in salt solutions. This resembles chemical etching in ocean water where minerals such as silica (SiO_2) and silicates dissolve over long time scales. While details of diameter etch rates vary and depend on parameters such as salt type and concentration (summarized in Table 1), our observation of pore etching and expansion in ambient conditions *without any voltage applied* is valid for a large range of diameters (2−80 nm), thicknesses (10−100 nm), and two different pore fabrication methods. Based on previous works on laser illumination of SiN_x membranes in salt solution,[16,42] parameters such as the Si:N ratio in the membrane, pH, and temperature are expected to affect this process. We note that pores can be formed by simple chemical etching in salt solution and in electron-irradiated membrane regions, and this phenomenon may be used as a practical pore-fabrication method, akin to electroporation,[32] but without voltage application. We further discovered that ethanol/water is a good candidate for long-term nanopore storage purposes.

We conclude by remarking an apparent trade-off arising between the ease of membrane thinning and pore formation, on the one hand, and their long-term stability and robustness, on the other. It appears that Si-rich SiN_x membrane regions may be good for easy pore formation in salt solution (for example by irradiation and/or electroporation), but they may be more susceptible to pore etching and expansion. To avoid etching altogether, a few nm-thick hafnium oxide coating, that can be as thin as 1 nm, provides a resistant layer that prevents long-term etching in salt solutions over periods of days.

MATERIALS AND METHODS

Nanopore Fabrication. Electron-transparent TEM windows are first fabricated in 5 × 5 mm^2 Si/SiO_2 chips coated with 100 nm of low-stress SiN_x (at Cornell Nanofabrication Facility (CNF)) using microfabrication processes described elsewhere.[11] The SiN_x membrane is then thinned to a thickness of 10 nm using CHF_3 and O_2 RIE. Nanopores are drilled *in situ* at room temperature with a JEOL F200 TEM operating in high-resolution mode with an acceleration voltage of 200 kV. The probe with a current of 20 nA is momentarily condensed to the beam crossover point on the SiN_x membrane for 5−10 s (total dose ~ 8.0×10^{11} e^-/nm^2) to form a pore. Prior to ionic current measurements, pores are exposed to boiling piranha solution (1:3 v/v H_2O_2:H_2SO_4) for 10 min, which removes organic contaminants and aids in pore wetting.[49] HfO_2 is deposited using Cambridge Nanotech S200 ALD system, with tetrakis(dimethylamino)hafnium (HFDMA) and H_2O, at 150 °C. Deposited thickness per cycle is calibrated at an average of 1.14 Å/cycle.[50] The thickness of the resulting pore is later confirmed from ionic conductance and the measured diameter, d_{TEM}.

Nanopore Array Fabrication. The SiN_x membrane is first spin-coated with 1:2 dilution of ZEP520A:Anisole at 4000 rpm for 40 s, followed by 2 min of baking at 180 °C. Array patterning is exposed onto the resist layer using Elionix ELS-7500EX with a shot pitch of 100 nm and a dose of 18 $\mu C/cm^2$. The resist is then developed in *o*-xylene for 70 s and isopropyl alcohol (IPA) for 30 s. Nanopore array is transferred into the SiN_x membrane *via* RIE, as described above. To strip off the resist, the membrane is placed in heated *N*-methyl-2-pyrrolidone (NMP) at 60 °C for 3 h and then rinsed with IPA.

Ionic Solution Storage. Unbuffered ionic solutions were produced by dissolving KCl, $MgCl_2$, and LiCl pellets (Alfa Aesar) in ultrapure deionized (DI) water at discrete concentrations of 0.01, 0.1, 1, and 3 M. EtOH:H_2O (v/v = 1/1) solutions were produced by mixing equal amounts of HPLC grade ethanol (Fisher Chemical) and DI water. Individual nanopores and nanopore arrays were stored in solutions at room temperature (25 °C) and ambient light, for up to 78 days in sealed containers to minimize atmospheric gas dissolution. Prior to ionic current measurements and TEM inspection, samples were flushed with DI water to remove residue ionic solution from storage and dried with clean N_2 gas, respectively.

Ionic Current Measurements. Ionic measurements were acquired using a VC100 amplifier (Chimera Instruments, New York, NY) and bias voltage is applied *via* a set of two-terminal Ag/AgCl electrodes. All measurements are conducted in unbuffered 1 M KCl (pH 8.0, σ = 11.1 S/m). Conductance is estimated from the current changes given a fixed step size of voltage bias. Applied voltages were kept below 0.1 V to prevent pore expansion and/or dielectric breakdown,[32] and during the measurement period of < 30 min, the conductance remained constant.

TEM Imaging. About 18 single pores were imaged by TEM to directly measure their diameter. First, the pore was drilled in the "TEM mode" of the F200 JEOL high-resolution TEM and then imaged to obtain the initial d_{TEM}. The pore was then removed from vacuum and cleaned with piranha, rinsed with DI water, and immersed in salt solution for some period of time, for example, for ~ 2 days. The pores were then taken out of solution, rinsed with DI water, dried with N_2 gas, and imaged in the TEM vacuum chamber to obtain a second TEM image of the pore, from which the new diameter was measured. The error in diameter measurement from these images is about 0.1 nm. Except for pore vii in Figure 3a, we did not perform conductance measurements on these pores to minimize chip handling in and out of salt solutions and possible chip failure modes.

TEM Image Analysis of RIE Pores in the Nanopore Array. Low-magnification TEM images of nanopore arrays were processed using ImageJ software. With the particle analysis feature, an enclosed nanopore area can be identified and obtained, owing to a phase contrast difference between the pore region and the SiN_x region. The d_{TEM} is then approximated from the total pore area equated to $\pi \times (d_{TEM}/2)^2$. A subset of 900 nanopores in Figure 4e, out of an approximate number of 150,000 nanopores, were randomly chosen from each TEM image inspection session to determine the average nanopore diameter after each consecutive storage time in ionic solution.

ADF Imaging and EELS Measurements. Before imaging, samples exposed to salt solution were annealed at 300 °C for 90 min in Ar/H_2. Dark-field images were acquired on a probe-corrected JEOL NEOARM operating at 200 kV with a high-angle annular dark-field (HAADF) detector. EELS spectra were acquired on a GIF Quantum Summit detector with a resolution of 0.5 eV. The 80−90 square pixel EELS maps were acquired with an acquisition time of 0.2−0.5 s/pixel.

ASSOCIATED CONTENT

Supporting Information

The Supporting Information is available free of charge at https://pubs.acs.org/doi/10.1021/acsnano.9b09964.

Full conductance data for the pore described in Figure 2c as well as images for individual TEM-drilled pores stored in both 1 M LiCl and 1 M $MgCl_2$. A study of KCl etching

https://dx.doi.org/10.1021/acsnano.9b09964
ACS Nano XXXX, XXX, XXX−XXX

in commercially available SiN_x membranes and additional ADF/EELS data for nanopore arrays are also provided. Lastly, we describe variations in nanopore diameter across EBL-patterned arrays in SiN_x membranes (PDF)

AUTHOR INFORMATION

Corresponding Author

Marija Drndić − *Department of Physics and Astronomy, University of Pennsylvania, Philadelphia, Pennsylvania 19104, United States;* orcid.org/0000-0002-8104-2231; Email: drndic@physics.upenn.edu

Authors

Yung-Chien Chou − *Department of Physics and Astronomy, University of Pennsylvania, Philadelphia, Pennsylvania 19104, United States;* orcid.org/0000-0001-6763-1657

Paul Masih Das − *Department of Physics and Astronomy, University of Pennsylvania, Philadelphia, Pennsylvania 19104, United States;* orcid.org/0000-0003-2644-2280

Dimitri S. Monos − *Department of Pathology and Laboratory Medicine, Perelman School of Medicine, University of Pennsylvania and The Children's Hospital of Philadelphia, Philadelphia, Pennsylvania 19104, United States; Immunogenetics Laboratory, Children's Hospital of Philadelphia, Philadelphia, Pennsylvania 19104, United States*

Complete contact information is available at: https://pubs.acs.org/10.1021/acsnano.9b09964

Author Contributions

‖Y.-C.C. and P.M.D contributed equally to this work. All authors designed the experiments. Y.-C.C. fabricated single nanopore and nanopore array samples. Y.-C.C. performed ionic current measurements. Y.-C.C. and P.M.D. conducted TEM imaging and analyzed TEM images. The manuscript was written through contributions of all authors. All authors have given approval to the final version of the manuscript.

Notes

The authors declare the following competing financial interest(s): M.D. is consultant and founder of Goeppert LLC (www.gppert.com), which is manufacturing nanotechnology-related products including solid-state nanopore chips and 2D membranes.

ACKNOWLEDGMENTS

This research was primarily supported by the NSF through the University of Pennsylvania Materials Research Science and Engineering Center (MRSEC) DMR-1720530 as well as NSF Grants EFRI 2-DARE 1542707, NSF DMR 1905045, and NSF EAGER 1838456, and NIH R21 HG010536 and institutional funds from The Children's Hospital of Philadelphia. This work was performed in part at the University of Pennsylvania's Singh Center for Nanotechnology, an NNCI member supported by NSF grant ECCS-1542153. We thank Dr. Douglas Yates and Dr. Hiromichi Yamamoto at the University of Pennsylvania for their generous help with TEM and EBL. We also thank Dr. David Niedzwiecki, Dr. Chen-Chi Chien, Prof. Meni Wanunu, and Jacob Swett for useful comments and/or discussion.

REFERENCES

(1) Dekker, C. Solid-State Nanopores. *Nat. Nanotechnol.* **2007**, *2*, 209−215.

(2) Kasianowicz, J. J.; Robertson, J. W. F.; Chan, E. R.; Reiner, J. E.; Stanford, V. M. Nanoscopic Porous Sensors. *Annu. Rev. Anal. Chem.* **2008**, *1*, 737−766.

(3) Storm, A. J.; Chen, J. H.; Ling, X. S.; Zandbergen, H. W.; Dekker, C. Fabrication of Solid-State Nanopores with Single-Nanometre Precision. *Nat. Mater.* **2003**, *2*, 537−540.

(4) Howorka, S.; Cheley, S.; Bayley, H. Sequence-Specific Detection of Individual DNA Strands Using Engineered Nanopores. *Nat. Biotechnol.* **2001**, *19*, 636−639.

(5) Clarke, J.; Wu, H. C.; Jayasinghe, L.; Patel, A.; Reid, S.; Bayley, H. Continuous Base Identification for Single-Molecule Nanopore DNA Sequencing. *Nat. Nanotechnol.* **2009**, *4*, 265−270.

(6) Szalay, T.; Golovchenko, J. A. De Novo Sequencing and Variant Calling with Nanopores Using PoreSeq. *Nat. Biotechnol.* **2015**, *33*, 1087−1091.

(7) Petrossian, L.; Wilk, S. J.; Joshi, P.; Goodnick, S. M.; Thornton, T. J. Demonstration of Coulter Counting through a Cylindrical Solid State Nanopore. *J. Phys.: Conf. Ser.* **2008**, *109*, 012028.

(8) Deamer, D. W.; Akeson, M. Nanopores and Nucleic Acids: Prospects for Ultrarapid Sequencing. *Trends Biotechnol.* **2000**, *18*, 147−151.

(9) Li, J.; Gershow, M.; Stein, D.; Brandin, E.; Golovchenko, J. A. DNA Molecules and Configurations in a Solid-State Nanopore Microscope. *Nat. Mater.* **2003**, *2*, 611−615.

(10) Lee, K.; Park, K. B.; Kim, H. J.; Yu, J. S.; Chae, H.; Kim, H. M.; Kim, K. B. Recent Progress in Solid-State Nanopores. *Adv. Mater.* **2018**, *30*, 1704680.

(11) Wanunu, M.; Dadosh, T.; Ray, V.; Jin, J.; McReynolds, L.; Drndić, M. Rapid Electronic Detection of Probe-Specific MicroRNAs Using Thin Nanopore Sensors. *Nat. Nanotechnol.* **2010**, *5*, 807−814.

(12) Merchant, C. A.; Healy, K.; Wanunu, M.; Ray, V.; Peterman, N.; Bartel, J.; Fischbein, M. D.; Venta, K.; Luo, Z.; Johnson, A. T. C.; Drndić, M. DNA Translocation through Graphene Nanopores. *Nano Lett.* **2010**, *10*, 2915−2921.

(13) Fragasso, A.; Schmid, S.; Dekker, C. Comparing Current Noise in Biological and Solid-State Nanopores. *ACS Nano* **2020**, *14*, 1338−1349.

(14) Chien, C. C.; Shekar, S.; Niedzwiecki, D. J.; Shepard, K. L.; Drndić, M. Single-Stranded DNA Translocation Recordings through Solid-State Nanopores on Glass Chips at 10 MHz Measurement Bandwidth. *ACS Nano* **2019**, *13*, 10545−10554.

(15) Rodríguez-Manzo, J. A.; Puster, M.; Nicolaï, A.; Meunier, V.; Drndić, M. DNA Translocation in Nanometer Thick Silicon Nanopores. *ACS Nano* **2015**, *9*, 6555−6564.

(16) Yamazaki, H.; Hu, R.; Zhao, Q.; Wanunu, M. Photothermally Assisted Thinning of Silicon Nitride Membranes for Ultrathin Asymmetric Nanopores. *ACS Nano* **2018**, *12*, 12472−12481.

(17) Venta, K.; Shemer, G.; Puster, M.; Rodríguez-Manzo, J. A.; Balan, A.; Rosenstein, J. K.; Shepard, K.; Drndić, M. Differentiation of Short, Single-Stranded DNA Homopolymers in Solid-State Nanopores. *ACS Nano* **2013**, *7*, 4629−4636.

(18) Li, J.; Stein, D.; McMullan, C.; Branton, D.; Aziz, M. J.; Golovchenko, J. A. Ion-Beam Sculpting at Nanometre Length Scales. *Nature* **2001**, *412*, 166−169.

(19) Verschueren, D. V.; Yang, W.; Dekker, C. Lithography-Based Fabrication of Nanopore Arrays in Freestanding SiN and Graphene Membranes. *Nanotechnology* **2018**, *29*, 145302.

(20) Isotalo, T. J.; Niemi, T. Dots-On-the-Fly Electron Beam Lithography. Proceedings from *SPIE: Alternative Lithographic Technologies VIII*, February 22−25, 2016, San Jose, CA; Bencher, C., Ed.; SPIE - International Society for Optics and Photonics: Bellingham, WA, 2016; Vol. *9777*.

(21) Kowalczyk, S. W.; Grosberg, A. Y.; Rabin, Y.; Dekker, C. Modeling the Conductance and DNA Blockade of Solid-State Nanopores. *Nanotechnology* **2011**, *22*, 315101.

(22) Kim, M. J.; McNally, B.; Murata, K.; Meller, A. Characteristics of Solid-State Nanometre Pores Fabricated Using a Transmission Electron Microscope. *Nanotechnology* **2007**, *18*, 205302.

https://dx.doi.org/10.1021/acsnano.9b09964
ACS Nano XXXX, XXX, XXX−XXX

(23) Madejski, G.; Lucas, K.; Pascut, F. C.; Webb, K. F.; McGrath, J. L. TEM Tomography of Pores with Application to Computational Nanoscale Flows in Nanoporous Silicon Nitride (NPN). *Membranes* **2018**, *8*, 26.
(24) Chen, C.-H.; Chang, X.; Wu, C.-S. A Novel Shaped-Controlled Fabrication of Nanopore and Its Applications in Quantum Electronics. *Sci. Rep.* **2019**, *9*, 18663.
(25) van den Hout, M.; Hall, A. R; Wu, M. Y.; Zandbergen, H. W; Dekker, C.; Dekker, N. H Controlling Nanopore Size, Shape and Stability. *Nanotechnology* **2010**, *21*, 115304.
(26) Wu, M.-Y.; Smeets, R. M. M.; Zandbergen, M.; Ziese, U.; Krapf, D.; Batson, P. E.; Dekker, N. H.; Dekker, C.; Zandbergen, H. W. Control of Shape and Material Composition of Solid-State Nanopores. *Nano Lett.* **2009**, *9*, 479−484.
(27) Li, Q.; Zhao, Q.; Lu, B.; Zhang, H.; Liu, S.; Tang, Z.; Qu, L.; Zhu, R.; Zhang, J.; You, L.; Yang, F.; Yu, D. Size Evolution and Surface Characterization of Solid-State Nanopores in Different Aqueous Solutions. *Nanoscale* **2012**, *4*, 1572−1576.
(28) Wanunu, M.; Meller, A. Chemically Modified Solid-State Nanopores. *Nano Lett.* **2007**, *7*, 1580−1585.
(29) Williams, K. R.; Gupta, K.; Wasilik, M. Etch Rates for Micromachining Processing-Part II. *J. Microelectromech. Syst.* **2003**, *12*, 761−778.
(30) Williams, K. R.; Muller, R. S. Etch Rates for Micromachining Processing. *J. Microelectromech. Syst.* **1996**, *5*, 256−269.
(31) Albrecht, T.; Gibb, T.; Nuttall, P. Ion Transport in Nanopores. In *Engineered Nanopores for Bioanalytical Applications*; Edel, J. B., Albrecht, T., Eds.; Micro and Nano Technologies; Elsevier Science: Norwich, NY, 2013; pp 7−12.
(32) Kwok, H.; Briggs, K.; Tabard-Cossa, V. Nanopore Fabrication by Controlled Dielectric Breakdown. *PLoS One* **2014**, *9*, No. e92880.
(33) Thompson, M. E. Glass Electrodes for Hydrogen and Other Cations. Principles and Practice. *Science* **1967**, *158*, 625.
(34) Khoshkbarchi, M. K.; Vera, J. H. Measurement and Correlation of Ion Activity Coefficients in Aqueous Solutions of Mixed Electrolyte with a Common Ion. *Fluid Phase Equilib.* **1996**, *121*, 253−265.
(35) Taghikhani, V.; Modarress, H.; Vera, J. H. Individual Anionic Activity Coefficients in Aqueous Electrolyte Solutions of LiCl and LiBr. *Fluid Phase Equilib.* **1999**, *166*, 67−77.
(36) Rodil, E.; Vera, J. H. Individual Activity Coefficients of Chloride Ions in Aqueous Solutions of $MgCl_2$, $CaCl_2$ and $BaCl_2$ at 298.2 K. *Fluid Phase Equilib.* **2001**, *187−188*, 15−27.
(37) Healy, K.; Ray, V.; Willis, L. J.; Peterman, N.; Bartel, J.; Drndić, M. Fabrication and Characterization of Nanopores with Insulated Transverse Nanoelectrodes for DNA Sensing in Salt Solution. *Electrophoresis* **2012**, *33*, 3488−3496.
(38) Puster, M.; Rodríguez-Manzo, J. A.; Balan, A.; Drndić, M. Toward Sensitive Graphene Nanoribbon−Nanopore Devices by Preventing Electron Beam-Induced Damage. *ACS Nano* **2013**, *7*, 11283−11289.
(39) Danda, G.; Masih Das, P.; Chou, Y.-C.; Mlack, J. T.; Parkin, W. M.; Naylor, C. H.; Fujisawa, K.; Zhang, T.; Fulton, L. B.; Terrones, M.; Johnson, A. T. C.; Drndić, M. Monolayer WS_2 Nanopores for DNA Translocation with Light-Adjustable Sizes. *ACS Nano* **2017**, *11*, 1937−1945.
(40) Liu, L.-H.; Michalak, D. J.; Chopra, T. P.; Pujari, S. P.; Cabrera, W.; Dick, D.; Veyan, J.-F.; Hourani, R.; Halls, M. D.; Zuilhof, H.; Chabal, Y. J. Surface Etching, Chemical Modification and Characterization of Silicon Nitride and Silicon Oxide—Selective Functionalization of Si_3N_4 and SiO_2. *J. Phys.: Condens. Matter* **2016**, *28*, 094014.
(41) Mackenzie, F. T.; Garrels, R. M.; Bricker, O. P.; Bickley, F. Silica in Sea Water: Control by Silica Minerals. *Science* **1967**, *155*, 1404−1405.
(42) Gilboa, T.; Zvuloni, E.; Zrehen, A.; Squires, A. H.; Meller, A. Automated, Ultra-Fast Laser-Drilling of Nanometer Scale Pores and Nanopore Arrays in Aqueous Solutions. *Adv. Funct. Mater.* **2019**, 1900642.
(43) Gilboa, T.; Zrehen, A.; Girsault, A.; Meller, A. Optically-Monitored Nanopore Fabrication Using a Focused Laser Beam. *Sci. Rep.* **2018**, *8*, 9765.
(44) Yamazaki, H.; Hu, R.; Henley, R. Y.; Halman, J.; Afonin, K. A.; Yu, D.; Zhao, Q.; Wanunu, M. Label-Free Single-Molecule Thermoscopy Using a Laser-Heated Nanopore. *Nano Lett.* **2017**, *17*, 7067−7074.
(45) Nicoli, F.; Verschueren, D.; Klein, M.; Dekker, C.; Jonsson, M. P. DNA Translocations through Solid-State Plasmonic Nanopores. *Nano Lett.* **2014**, *14*, 6917−6925.
(46) Danda, G.; Masih Das, P.; Drndić, M. Laser-Induced Fabrication of Nanoporous Monolayer WS_2 Membranes. *2D Mater.* **2018**, *5*, 035011.
(47) Di Fiori, N.; Squires, A.; Bar, D.; Gilboa, T.; Moustakas, T. D.; Meller, A. Optoelectronic Control of Surface Charge and Translocation Dynamics in Solid-State Nanopores. *Nat. Nanotechnol.* **2013**, *8*, 946−951.
(48) Venkatesan, B. M.; Shah, A. B.; Zuo, J. M.; Bashir, R. DNA Sensing Using Nanocrystalline Surface-Enhanced Al_2O_3 Nanopore Sensors. *Adv. Funct. Mater.* **2010**, *20*, 1266−1275.
(49) Niedzwiecki, D. J.; Movileanu, L. Monitoring Protein Adsorption with Solid-State Nanopores. *J. Visualized Exp.* **2011**, *58*, e3560.
(50) Metzler, M.; Lu, Y. *Atomic Layer Deposition (ALD) Film Characterization; Tool data. Paper 33*; ScholarlyCommons: Philadelphia, PA, 2016; pp 2−3.

https://dx.doi.org/10.1021/acsnano.9b09964
ACS Nano XXXX, XXX, XXX−XXX